Challa S.S.R. Kumar *Editor*

X-ray and Neutron Techniques for Nanomaterials Characterization

MATERIALS.SPRINGER.COM

Springer

X-ray and Neutron Techniques for Nanomaterials Characterization

Challa S. S. R. Kumar
Editor

X-ray and Neutron Techniques for Nanomaterials Characterization

With 328 Figures and 19 Tables

Springer

Editor
Challa S. S. R. Kumar
Integrated Mesoscale Architectures for
Sustainable Catalysis (IMASC)
Rowland Institute of Science
Harvard University
Cambridge, MA, USA

ISBN 978-3-662-48604-7 ISBN 978-3-662-48606-1 (eBook)
DOI 10.1007/978-3-662-48606-1

Library of Congress Control Number: 2016948851

Printed on acid-free paper

This Springer imprint is published by Springer Nature
The registered company is Springer-Verlag GmbH Germany
The registered company address is: Heidelberger Platz 3, 14197 Berlin, Germany

Contents

Contributors

Kiyotaka Asakura Catalysis Research Center, Hokkaido University, Sapporo, Hokkaido, Japan

Kyoko Bando Nanosystem Research Institute, National Institute of Advanced Industrial Science and Technology (AIST), Tsukuba, Japan

Loïc Barré IFP Energies Nouvelles, Rueil Malmaison, France

Oier Bikondoa Department of Physics, University of Warwick, Coventry, UK

XMaS, The UK-CRG Beamline, ESRF – The European Synchrotron, Grenoble, France

Lisa Bovenkamp-Langlois CAMD (Center for Advanced Microstructures and Devices), Louisiana State University, Baton Rouge, LA, USA

Center for Atomic-Level Catalyst Design, Cain Department of Chemical Engineering, Louisiana State University, Baton Rouge, LA, USA

Antonio Cervellino Swiss Light Source, Paul Scherrer Institut, Villigen, Switzerland

Suresh M. Chathoth Department of Physics and Materials Science, City University of Hong Kong, Kowloon Tong, Hong Kong

Wang-Jae Chun Graduate School of Arts and Sciences, International Christian University, Mitaka, Tokyo, Japan

Ruggero Frison Istituto di Cristallografia and To.sca.Lab., Consiglio Nazionale delle Ricerche, Como, Italy

Department of Chemistry, University of Zurich, Zurich, Switzerland

Alexandre Giuliani Synchrotron SOLEIL, L'Orme des Merisiers, Gif-sur-Yvette, France

UAR1008, CEPIA, INRA, Nantes, France

Antonietta Guagliardi Istituto di Cristallografia and To.sca.Lab., Consiglio Nazionale delle Ricerche, Como, Italy

Yuriy Halahovets Institute of Physics, Slovak Academy of Sciences, Bratislava, Slovakia

Bernhard Hesse ESRF – The European Synchrotron, Grenoble, France

Adam Hitchcock Department of Chemistry and Chemical Biology, McMaster University, Hamilton, ON, Canada

Martin Hodas Institute of Physics, Slovak Academy of Sciences, Bratislava, Slovakia

Matej Jergel Institute of Physics, Slovak Academy of Sciences, Bratislava, Slovakia

Maria Katsikini School of Physics, Department of Solid State Physics, Aristotle University of Thessaloniki, Thessaloniki, Greece

Toshihiro Kondo Global Research Center for Environment and Energy based on Nanomaterials Science (GREEN), National Institute for Materials Science (NIMS), Tsukuba, Japan

Graduate School of Humanities and Sciences, Ochanomizu University, Bunkyo-ku, Tokyo, Japan

Dusan Korytar Institute of Electrical Engineering, Slovak Academy of Sciences, Bratislava, Slovakia

Max Langer CREATIS, CNRS UMR5220, Inserm U1206, Université de Lyon, INSA-Lyon, Université Claude Bernard Lyon 1, Villeurbanne, France

ESRF – The European Synchrotron, Grenoble, France

Eva Majkova Institute of Physics, Slovak Academy of Sciences, Bratislava, Slovakia

Nebojsa Marinkovic Department of Chemical Engineering, Columbia University, New York, NY, USA

Norberto Masciocchi Dipartimento di Scienza e Alta Tecnologia and To.sca.Lab., Università dell'Insubria, Como, Italy

Takuya Masuda Global Research Center for Environment and Energy based on Nanomaterials Science (GREEN), National Institute for Materials Science (NIMS), Tsukuba, Japan

Advanced Key Technologies Division, National Institute for Materials Science (NIMS), Tsukuba, Japan

Precursory Research for Embryonic Science and Technology (PRESTO), Japan Science and Technology Agency (JST), Kawaguchi, Japan

Aleksandar R. Milosavljević Institute of Physics Belgrade, University of Belgrade, Belgrade, Serbia

Christophe Nicolas Synchrotron SOLEIL, L'Orme des Merisiers, Gif-sur-Yvette, France

Martin Obst Bayreuth Center of Ecology and Environmental Research (BayCEER), University of Bayreuth, Bayreuth, Germany

Eleni C. Paloura School of Physics, Department of Solid State Physics, Aristotle University of Thessaloniki, Thessaloniki, Greece

Marco Pelletta Institute of Physics, Slovak Academy of Sciences, Bratislava, Slovakia

Kotaro Sasaki Chemistry Department, Brookhaven National Laboratory, Upton, NY, USA

Martha W. Schaefer CAMD (Center for Advanced Microstructures and Devices), Louisiana State University, Baton Rouge, LA, USA

Department of Geology and Geophysics, Louisiana State University, Baton Rouge, LA, USA

Department of Physics and Astronomy, Louisiana State University, Baton Rouge, LA, USA

Gregor Schmid Center for Applied Geoscience, Eberhard Karls University Tuebingen, Tuebingen, Germany

Peter Siffalovic Institute of Physics, Slovak Academy of Sciences, Bratislava, Slovakia

Satoru Takakusagi Catalysis Research Center, Hokkaido University, Sapporo, Hokkaido, Japan

Hiroyuki Takeno Department of Chemistry and Chemical Biology, School of Science and Technology, Gunma University, Kiryu, Gunma, Japan

Madhusudan Tyagi NIST Center for Neutron Research, Gaithersburg, MD, USA

Department of Materials Science and Engineering, University of Maryland, College Park, MD, USA

Yohei Uemura Division of Electronic Structure, Department of Materials Science, Institute for Molecular Science, Okazai, Aichi, Japan

Kohei Uosaki Global Research Center for Environment and Energy based on Nanomaterials Science (GREEN), National Institute for Materials Science (NIMS), Tsukuba, Japan

International Center for Materials Nanoarchitectonics (MANA), National Institute for Materials Science (NIMS), Tsukuba, Japan

Peter Varga Julius-Wolff-Institute & Berlin Brandenburg School for Regenerative Therapies, Charité-Universitätsmedizin Berlin, Berlin, Germany

AO Research Institute Davos, Davos, Switzerland

Karol Vegso Institute of Physics, Slovak Academy of Sciences, Bratislava, Slovakia

Loriane Weber CREATIS, CNRS UMR5220, Inserm U1206, Université de Lyon, INSA-Lyon, Université Claude Bernard Lyon 1, Villeurbanne, France

ESRF – The European Synchrotron, Grenoble, France

Juan Wu Department of Chemistry and Chemical Biology, McMaster University, Hamilton, ON, Canada

Zdeno Zaprazny Institute of Electrical Engineering, Slovak Academy of Sciences, Bratislava, Slovakia

Synchrotron X-Ray Phase Nanotomography for Bone Tissue Characterization

1

Peter Varga, Loriane Weber, Bernhard Hesse, and Max Langer

Contents

P. Varga (✉)
Julius-Wolff-Institute & Berlin Brandenburg School for Regenerative Therapies, Charité-Universitätsmedizin Berlin, Berlin, Germany

AO Research Institute Davos, Davos, Switzerland
e-mail: peter.varga@aofoundation.org

L. Weber • M. Langer
CREATIS, CNRS UMR5220, Inserm U1206, Université de Lyon, INSA-Lyon, Université Claude Bernard Lyon 1, Villeurbanne, France

ESRF – The European Synchrotron, Grenoble, France
e-mail: loriane.weber@esrf.fr; max.langer@esrf.fr

B. Hesse
ESRF – The European Synchrotron, Grenoble, France
e-mail: bernhard.hesse@esrf.fr

C.S.S.R. Kumar (ed.), *X-ray and Neutron Techniques for Nanomaterials Characterization*, DOI 10.1007/978-3-662-48606-1_1

1 Definition of the Topic

X-ray phase nano-tomography allows the characterisation of bone ultrastructure: the lacuno-canalicular network, nanoscale mineralisation and the collagen orientation. In this chapter, we review the different X-ray imaging techniques capable of imaging the bone ultrastructure and then describe the work that has been done so far in nanoscale bone tissue characterisation using X-ray phase nano-tomography.

2 Overview

X-ray computed tomography at the micrometric scale is more and more considered as the reference technique in imaging of bone microstructure. The trend has been to push towards higher and higher resolution. Due to the difficulty of realising optics in the hard X-ray regime, the magnification has mainly been due to the use of visible light optics and indirect detection of the X-rays, which limits the attainable resolution with respect to the wavelength of the visible light used in detection. Recent developments in X-ray optics and instrumentation have allowed the implementation of several types of methods that achieve imaging limited in resolution by the X-ray wavelength, thus enabling computed tomography at the nanoscale. We review here the X-ray techniques with 3D imaging capability at the nanoscale: transmission X-ray microscopy, ptychography and in-line holography. Then, we present the experimental methodology for the in-line phase tomography, both at the instrumentation level and the physics behind this imaging technique. Further, we review the different ultrastructural features of bone that have so far been resolved and the applications that have been reported: imaging of the lacuno-canalicular network, direct analysis of collagen orientation, analysis of mineralisation on the nanoscale and the use of 3D images at the nanoscale as the basis of mechanical analyses. Finally, we discuss the issue of going beyond qualitative description to quantification of ultrastructural features.

3 Introduction

X-ray imaging and assessment of bone have been intimately linked already since the discovery of X-rays. Actually, the first application of X-rays was visualisation of bone on the organ level [1]. This consisted in simple projection images, usually known as radiographs. X-ray computed tomography (CT) [2, 3], that is, cross-sectional imaging, enables three-dimensional (3D) imaging by combining the acquisition of radiographs at several angles of rotation around the targeted object and a tomographic reconstruction algorithm. This modality has gained wide use in medical imaging. X-ray CT at the micron scale (μCT) combines CT imaging with the use of high-resolution detectors. X-ray μCT has recently assumed the place as the reference method for bone microstructure imaging, among other applications [4]. This is, apart from the excellent contrast in hard materials, sufficient penetration in bone and 3D

nature of the images, due to compact μCT systems being increasingly available [5–7]. Synchrotron sources in combination with insertion devices are powerful X-ray sources enabling highly monochromatic X-rays. If such a source is used, the resulting modality is called synchrotron radiation μCT (SR-μCT) [8] that allows functional imaging, i.e. direct 3D quantification of the degree of mineralisation of bone (DMB) at the micro-scale [9].

The trend in μCT and other X-ray microscopy techniques has been to go towards higher and higher resolution [10], since the properties of X-rays are very appealing: short wavelength (so a lower diffraction limit than with visible light) combined with high penetration power yielding good contrast in bone. This goes hand in hand with the increasing demand of quantitative 3D images of bone at the micro- and nano-scale, due to the links between ultrastructure and failure [11, 12]. The high penetration power makes it difficult to implement X-ray focusing optics, however, which has kept the magnification factor due to the X-ray beam fairly low. High-resolution imaging has instead been achieved by indirect detection: a fluorescent screen, a scintillator with a high efficiency in converting X-rays to visible light, imaged by standard visible light microscope optics onto a CCD camera [13]. This kind of system is diffraction limited in resolution by the wavelength of the visible light emitted by the scintillator, however. In this case, imaging of the ultrastructure cannot be considered, since this is usually reserved for features that are smaller than those resolvable with a standard bright field visible light microscope operating in transmission mode.

Osteoporosis and other bone fragility-related diseases are not yet fully understood and are thus the subject of active research. While previously the main focus was the characterisation, description and diagnosis of these diseases, currently the main aim is to uncover the mechanisms behind bone loss and those involved in bone failure. Bone mass is the most important determinant of bone strength, but it is known not to be the only factor. For example, collagen cross-linking is thought to be important for the integrity of the bone tissue [14]. Bone fragility is thought to result from failed material or structural adaptations to mechanical stress [15]. Since bone adapts to externally imposed mechanical stresses through a process of remodelling, the bone tissue changes its macro-, micro- and ultrastructure during its lifetime.

Bone remodelling is achieved via the processes of mechanosensation and mechanotransduction, which are thought to be performed by the osteocyte system. Osteocytes are the most abundant bone cells dispersed throughout the bone system. They differentiate from osteoblasts, which are the cells responsible for bone formation, by getting trapped in the pre-bone matrix during tissue formation. The osteocytes interconnect and communicate through dendritic processes [16–19]. The imprint of osteocytes and their processes are called the lacunae and the canaliculi, respectively, and form the lacuno-canalicular network (LCN) [20]. The sensitivity of osteocytes to external strain could be due to sensing substrate deformation directly or by strains induced by the flow of interstitial fluid circulating in the LCN [21–23]. Moreover, microcracks are also thought to trigger remodelling by interrupting osteocyte dendrites [24–27]. The interest in studying osteocytes and their pore network has been on the rise the last few years, which can be witnessed by

published statements such that the LCN is "the unrecognized side of bone tissue" or that osteocytes "can't hide forever" [28–32]. Apart from their presumed role in the bone remodelling, these cells are also thought to contribute to the maintenance of mineral homeostasis. In relation to this, they secrete a number of biochemical factors, of which some are seen as potential therapeutic targets [33]. It should be mentioned however that the complete role of the osteocyte, and other possible processes for bone remodelling, is not yet fully elucidated but is rather the topic of active research [34].

Osteocytes and the LCN are not the only aspects of bone ultrastructure that are interesting to study, however. At the ultrastructural level, bone tissue is a natural nanocomposite consisting of mineralised collagen fibres. These fibres are organised in a regular fashion around the vessel canals: the Haversian canals forming the centre in units of bone remodelling called osteons and Volkmann canals interconnecting the Haversian canals and the periosteum. During the lifetime of bone tissue, mineralised matrix is being resorbed by osteoclasts and replaced by osteoblasts with new osteons. Between these secondary osteons, there remain rests of older tissue called interstitial tissue. At the boundary of each osteon, there is a layer of mineralised tissue called the cement line, which is thought to have an important role in limiting crack propagation and to affect the overall stiffness of bone [35, 36]. The cement line has previously been characterised mainly using quantitative backscatter electron imaging (qBEI). It has been disputed whether the cement line is hypo-mineralised [35, 36] or hyper-mineralised [37, 38]. It may also act as a boundary of the interconnected porosity within an osteon. At least one study has reported canalicular tunnelling through the cement line, however [39].

The organisation of the collagen fibrils is thought to directly influence bone strength and toughness. The analysis of collagen orientation has so far been performed mainly in 2D using scanning electron microscopy [40–43], transmission electron microscopy [44] and atomic force microscopy [45] or indirectly analysed by polarised light microscopy [46] and Raman spectral mapping [47, 48]. So far very little data is available on the 3D fine structure of the LCN and the bone matrix on the nanoscale. X-ray μCT has been used extensively to study bone tissue microstructure. There has been some work performed on imaging the LCN using μCT [49–55]. Since the diameter of the canaliculi can be as small as ~100 nm, μCT cannot by definition be used to image ultrastructure however, as mentioned above.

The techniques used to image bone ultrastructure in 3D have so far been transmission electron microscopy, scanning electron microscopy and confocal laser scanning microscopy (CLSM). CLSM is however limited by the depth of penetration in mineralised tissue, and its spatial resolution is anisotropic, depending on the depth into the sample where the focus is placed. It is also a scanning technique, which implies that data acquisition is relatively slow. Finally, advanced staining and sample preparation is necessary [56].

Another technique which has recently been progressing towards chemical imaging of bone ultrastructure is infrared nanoscopy. Even though this technique gives only access to the chemical properties in 2D, it might be of increasing interest due to

the increasing number of available instruments, relatively simple sample preparation and high spatial resolution up to tens of nm at a field of view in the order of 100 × 100 μm [57, 58].

Serial sectioning using a focused ion beam followed by imaging with scanning electron microscopy (FIB-SEM) to image the lacuno-canalicular network has been reported [42, 43, 59, 60]. While this technique offers excellent spatial resolution, it is a destructive technique, and it requires advanced sample preparation. The repeated sectioning and imaging also lead to long acquisition times. Finally, transmission electron tomography has been used to image osteocyte ultrastructure in situ [61]. However, this kind of imaging is limited to very thin sections, 3 μm in the cited work. Thus, the 3D information is quite limited and only provides a very local visualisation of the osteocyte.

We review here the work that has been done in imaging of the ultrastructure of bone in 3D using X-rays. We give a brief introduction to high-resolution X-ray imaging physics. We then continue to describe the different imaging methods that have been used for ultrastructural imaging in bone, along with the results that were obtained. We give particular attention to the propagation-based technique, where we outline more in detail the image formation and reconstruction. We then describe the type of analyses that have so far been possible at shorter length scales than can be seen by visible light. Finally, we briefly discuss what we consider the next step of 3D ultrastructure imaging in bone: the possibility of in situ cell imaging in bone using X-ray phase nano-tomography.

4 Experimental and Instrumental Methodology

4.1 Instrumentation

4.1.1 X-Ray Source

The work described in Sects. 5.1.3, 5.2, 5.3 and 5.4 was performed on beamline ID22 at the European Synchrotron Radiation Facility (ESRF), Grenoble, France. ID22 is located on a high-β straight section and was equipped with two insertion devices: an in-vacuum U23 and a revolver U35/U19. The electron beam in the synchrotron had a current of ~200 mA, an energy of 6 GeV and a relative energy spread of 0.001. The vertical (horizontal) emittance, β values and dispersion were 39 pm (3.9 nm), 3 m (37.2 m) and 0 m (0.137 m), respectively. The revolver device was chosen to give maximum photon output in a moderately narrow energy range centred on 17.5 keV, which is the principal working energy for imaging at ID22 [62].

4.1.2 X-Ray Optics

The X-ray focusing optics consisted of two graded multilayer coated mirrors mounted in a crossed Kirkpatrick-Baez (KB) configuration [63]. The vertical mirror was 112 mm long and had a focusing distance of 180 mm, and the horizontal mirror was 76 mm long and had a focusing distance of 83 mm. The mirrors were

dynamically bendable to create the appropriate elliptical shape required to focus the X-ray beam. The resulting reflectivity at 17 keV was 73 % and yielded a spot size of approximately 50 nm × 50 nm. The vertical mirror images directly the undulator source (~25 μm FWHM), whereas in the horizontal direction, a virtual source is created by the use of high heat-load slits. The multilayer mirrors both focus and monochromatise the beam, resulting in a very high flux of about 5×10^{12} photons/s and a moderate degree of monochromaticity of $\Delta E/E \approx 10^{-2}$ [64–68].

4.2 Image Formation

The refractive index n of an object can be described as [69]:

$$n(x, y, z) = 1 - \delta(x, y, z) + i\beta(x, y, z), \tag{1.1}$$

where δ is the refractive index decrement, related to the phase shift of the incident wave after passing through the sample, and β is the absorption index, related to the attenuation of the incident beam induced by the sample.

The refractive index decrement δ and the absorption index β can be respectively expressed as [69]

$$\delta = \frac{r_c \lambda^2}{2\pi} \rho_e \tag{1.2}$$

and

$$\beta = \frac{r_c \lambda^3 \rho_e}{4\pi^2 c} \sum_j \frac{f_j \gamma_j}{Z}, \tag{1.3}$$

where r_c denotes the classical electron radius, λ the wavelength of the X-ray beam, ρ_e the electron density, c the light velocity, f_j the number of electrons per atom with damping constant γ_j and Z the atomic number that corresponds to the total number of electrons per atom. Here, j corresponds to an electron in the atom.

The absorption index β is related to the attenuation coefficient μ by the following relationship [70]:

$$\mu(x, y) = \frac{4\pi}{\lambda} \int \beta(x, y, z) dz. \tag{1.4}$$

The attenuation B and phase shift φ induced by the object can be described as projections parallel to the propagation direction (here, the z-axis). Note that **x** represents the vector (x, y).

$$B(\mathbf{x}) = \frac{2\pi}{\lambda}\int \beta(\mathbf{x}, z)\, dz \tag{1.5}$$

and

$$\varphi(\mathbf{x}) = -\frac{2\pi}{\lambda}\int \delta(\mathbf{x},\ z)\, dz. \tag{1.6}$$

At each angle θ, the interaction between the object and the X-ray wave can be described as a transmittance function:

$$T_\theta(\mathbf{x}) = \exp(-B_\theta(\mathbf{x}) + i\varphi_\theta(\mathbf{x})). \tag{1.7}$$

Thus, if $u_{inc}(\mathbf{x})$ denotes the incident wave front and $u_0(\mathbf{x})$ the wave front right after the sample (i.e. for a null propagation distance), we obtain

$$u_0(\mathbf{x}) = T_\theta(\mathbf{x})u_{inc}(\mathbf{x}). \tag{1.8}$$

The corresponding intensity recorded by the detector, without any propagation, is

$$I_0(\mathbf{x}) = |u_0(\mathbf{x})|^2 \tag{1.9}$$

$$I_0(\mathbf{x}) = |T_\theta(\mathbf{x})u_{inc}(\mathbf{x})|^2 \tag{1.10}$$

$$I_0(\mathbf{x}) = \left|e^{-B_\theta(\mathbf{x})}e^{i\,\varphi_\theta(\mathbf{x})}u_{inc}(\mathbf{x})\right|^2 = \left|e^{-B_\theta(\mathbf{x})}\right|^2\left|e^{i\,\varphi_\theta(\mathbf{x})}\right|^2|u_{inc}(\mathbf{x})|^2 \tag{1.11}$$

$$I_0(\mathbf{x}) = e^{-2.B_\theta(\mathbf{x})}|u_{inc}(\mathbf{x})|^2 = e^{-2B_\theta(\mathbf{x})}I_{inc}(\mathbf{x}). \tag{1.12}$$

The free-space propagation over a distance D can be modelled by the Fresnel transform involving the propagator P_D [71]:

$$P_D(\mathbf{x}) = \frac{1}{i\lambda D}\exp\left(i\frac{\pi}{\lambda D}|\mathbf{x}|^2\right) \tag{1.13}$$

and its Fourier transform:

$$\tilde{P}_D(\mathbf{f}) = \exp\left(-i\pi\lambda D|\mathbf{f}|^2\right), \tag{1.14}$$

where $\mathbf{f} = (f, g)$ are the conjugate variables corresponding to $\mathbf{x}$.

Usually, in computer implementations, the propagator is applied in the Fourier domain, since there it becomes a multiplication instead of a convolution in the spatial domain. Mathematically, if $u_0(\mathbf{x})$ and $u_D(\mathbf{x})$ respectively denote the wave fronts right after the sample and at a distance D from the sample, we obtain

$$u_D(\mathbf{x}) = P_D(\mathbf{x}) * u_0(\mathbf{x}), \tag{1.15}$$

in the spatial domain, which corresponds to

$$\tilde{u}_D(\mathbf{f}) = \tilde{P}_D(\mathbf{f})\tilde{u}_0(\mathbf{f}) \tag{1.16}$$

in the Fourier domain.

Since u_D usually stays in the real domain, and the propagator is applied in the Fourier domain, we get

$$u_D(\mathbf{x}) = \mathcal{F}^{-1}\tilde{P}_D\mathcal{F}[u_0](\mathbf{x}). \tag{1.17}$$

The operator

$$\mathcal{F}r_D = \mathcal{F}^{-1}\tilde{P}_D\mathcal{F} \tag{1.18}$$

is called the Fresnel transform. If we assume flat illumination, the interaction between the incident wave front and the sample followed by free-space propagation over a distance D can be modelled by

$$T_{\theta,D}(\mathbf{x}) = (T_\theta * P_D)(\mathbf{x}). \tag{1.19}$$

The intensity recorded by the detector at a distance D is

$$I_{\theta,D}(\mathbf{x}) = \left|T_{\theta,D}(\mathbf{x})\right|^2. \tag{1.20}$$

In the Fourier domain, the intensity can be expressed as

$$\tilde{I}_D(\mathbf{f}) = \int T\left(\mathbf{x} - \frac{\lambda D\mathbf{f}}{2}\right)T^*\left(\mathbf{x} + \frac{\lambda D\mathbf{f}}{2}\right)\exp(-i2\pi\mathbf{x}\cdot\mathbf{f})d\mathbf{x}. \tag{1.21}$$

Thus, images recorded by the detector are quantitatively related to the phase shift of the wave induced by the object.

Holotomography consists in acquiring projections for a complete rotation of the sample, at different sample-to-detector distances. This enables to cover well the Fourier domain (the Fresnel transform can have zero crossing at certain distances).

4.2.1 Magnified Images Formation

Since the beam is divergent, recording an image at sample-to-detector distance D also induces, apart from phase contrast, magnification of the projections and creates a spherical wave front (Fig. 1.1). The magnification M is expressed using the well-known Thales' theorem:

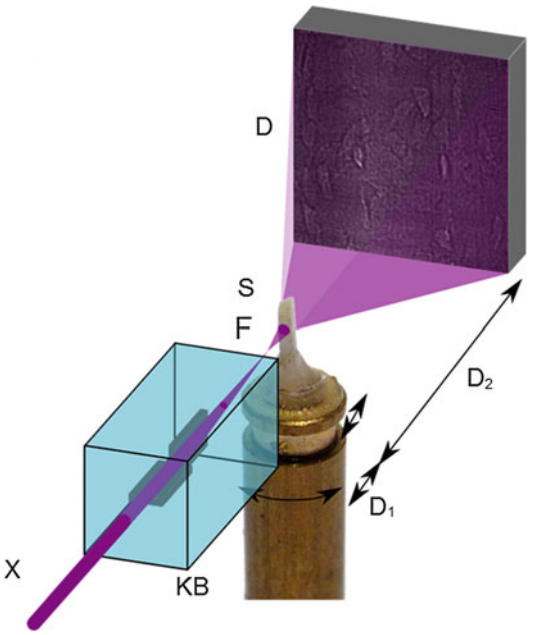

Fig. 1.1 The incoming parallel X-ray beam (X) is focused onto a focal spot (F) using Kirkpatrick-Baez mirrors, curved reflective optics that will horizontally and vertically focus the beam. D_1 represents the distance between the spot (F) and the sample (S). D_2 denotes the propagation distance, i.e. the distance between the sample and the detector [72]

$$M = \frac{D_1 + D_2}{D_1}. \tag{1.22}$$

We obtain projections with different magnification by modifying the propagation distance. In practice, the detector and the focus point are fixed, i.e. $D_1 + D_2$ is constant. It means that it is the sample that moves along a translation stage to get images with different magnifications.

Note that the spherical wave Fresnel diffraction phenomenon can be seen as a plane-wave illumination problem at the defocusing distance D defined by

$$\frac{1}{D} = \frac{1}{D_1} + \frac{1}{D_2}$$

$$\leftrightarrow D = \frac{D_1 D_2}{D_1 + D_2}$$

$$\leftrightarrow D = \frac{D_2}{M}. \tag{1.23}$$

In the following, D denotes the defocusing distance and can be seen as an equivalent of the propagation distance that takes into account the magnification.

Since the position of the focus and the detector are kept fixed, $[D_1, D_2, D_n, \ldots, D_N]$ represents the equivalent propagation distance indexed by n, with N the total number of distances used.

4.3 Phase Retrieval

4.3.1 Contrast Transfer Function

To retrieve the phase information from the image recorded by the detector (which is a non-linear problem), and since we are in the Fresnel diffraction regime, we can use the contrast transfer function (CTF) model. This linear model, which expresses the intensity as a linear function of the absorption and the refractive index decrement, is valid for slowly varying phase and weakly absorbing objects. These two conditions can be mathematically written as

$$|\varphi(\mathbf{x}) - \varphi(\mathbf{x} + \lambda D\mathbf{f})| \ll 1 \tag{1.24}$$

for slowly varying phase and

$$B(\mathbf{x}) \ll 1 \tag{1.25}$$

for weak absorption.

The CTF is based on the linearisation of the transmittance function to the first order:

$$T(\mathbf{x}) \approx 1 - B(\mathbf{x}) + i\varphi(\mathbf{x}). \tag{1.26}$$

By substituting the linearisation of the transmittance function in Eq. 1.21 and keeping only the first-order terms, we get the CTF:

$$\tilde{I}_D(\mathbf{f}) = \delta_{Dirac}(\mathbf{f}) - 2\cos\left(\pi\lambda D|\mathbf{f}|^2\right)\tilde{B}(\mathbf{f}) + 2\sin\left(\pi\lambda D|\mathbf{f}|^2\right)\tilde{\varphi}(\mathbf{f}), \tag{1.27}$$

Where ~ denotes the Fourier transform and δ_{Delta} the Dirac delta function.

Nevertheless, for nano-tomography, the propagation distances are relatively long compared to the pixel size and wavelength. This means the condition in Eq. 1.24 and thus the linearisation in Eq. 1.26 are no longer valid, so that the non-linear contribution of the phase cannot be neglected [73].

The CTF can be rewritten to take this into account:

$$\tilde{I}_D(\mathbf{f}) = \delta_{Dirac}(\mathbf{f}) - 2\cos\left(\pi\lambda D|\mathbf{f}|^2\right)\tilde{B}(\mathbf{f}) + 2\sin\left(\pi\lambda D|\mathbf{f}|^2\right)\tilde{\varphi}(\mathbf{f}) + \tilde{I}_{NL,D}(\mathbf{f}), \tag{1.28}$$

where $\tilde{I}_{NL,D}(\mathbf{f})$ represents the non-linear contribution.

Phase retrieval is thus performed in two stages. An initial guess of the phase is determined using a classical linear least square minimisation using the CTF, described in Sect. 4.3.2. This first guess corresponds to the linear part of the retrieved phase, but is not sufficient to provide good image quality at such high resolution. After, the non-linear term is determined using a non-linear iterative method, for example, a non-linear conjugate gradient algorithm [72].

4.3.2 Phase Retrieval with the CTF

To retrieve the phase using the CTF, linear least square optimisation is used. This method is usually used to solve an overdetermined problem, for example, a problem containing one unknown and N equations, as it is the case here, since we recorded images at N distances (that constitute our N equations) and want to determine one unknown, the phase.

Consider the following overdetermined problem:

$$y_n = A_n x + \varepsilon_n, \tag{1.29}$$

where n is an integer so that $n \in [1 : N]$, x is the unknown, y_n denotes one of the N measurements and A_n is the linear transformation applied to x to get y_n. The linear least square method determines an estimate of x, $\hat{x}$, so that

$$\frac{1}{N}\sum_{n=1}^{N} A_n^2 \hat{x} = \frac{1}{N}\sum_{n=1}^{N} A_n y_n. \tag{1.30}$$

Solving CTF (Eq. 1.27) is equivalent to minimise

$$\sum_{n=1}^{N} \left| 2\sin\left(\pi\lambda D_n |\mathbf{f}|^2\right)\tilde{\varphi}(\mathbf{f}) - 2\cos\left(\pi\lambda D_n |\mathbf{f}|^2\right)\tilde{B}(\mathbf{f}) - \tilde{I}_{D_n}(\mathbf{f}) \right|^2. \tag{1.31}$$

Here, Tikhonov regularisation is used to solve this minimisation problem [74]:

$$\hat{\tilde{\varphi}}(\mathbf{f}) = \frac{\left[K_{aa}\sum_{n=1}^{N} 2\sin\left(\pi\lambda D_n |\mathbf{f}|^2\right)\tilde{I}_{D_n}(\mathbf{f}) - K_{ap}\sum_{n=1}^{N} 2\cos\left(\pi\lambda D_n |\mathbf{f}|^2\right)\tilde{I}_{D_n}(\mathbf{f})\right]}{K_{aa}K_{pp} - K_{ap^2}} \tag{1.32}$$

with

$$K_{aa} = \sum_{n=1}^{N}\left(2\cos\left(\pi\lambda D_n |\mathbf{f}|^2\right)\right)^2 \tag{1.33}$$

$$K_{ap} = \sum_{n=1}^{N} 2\cos\left(\pi\lambda D_n |\mathbf{f}|^2\right) 2\sin\left(\pi\lambda D_n |\mathbf{f}|^2\right) \tag{1.34}$$

$$K_{pp} = \sum_{n=1}^{N}\left(2\sin\left(\pi\lambda D_n |\mathbf{f}|^2\right)\right)^2. \tag{1.35}$$

Once the projections are well conditioned, phase retrieval is performed according to the scheme presented above. A linear least square method is performed to assess roughly the phase and a non-linear conjugate gradient method to refine it. The obtained phase projections are eventually used as an input of a tomographic reconstruction algorithm (here, the filtered back projection method) to get a volume of the refractive index decrement.

5 Key Research Findings

5.1 Literature Review: X-Ray Nano-tomography of Bone

We review here the imaging methods that have so far been used to image bone ultrastructure at higher than 400 nm spatial resolution and the results that were obtained. To achieve such resolutions, advanced X-ray microscopy methods have to be used, where some magnification has to be implemented on the X-ray beam. This is not straightforward, however, as mentioned above, since the very small deviation from unity of the refractive index for X-rays makes it difficult to implement X-ray optics. The methods are surprisingly heterogeneous in their design, relying on attenuation and far-field and near-field diffraction, respectively.

5.1.1 Ptychographic Tomography

One way to achieve high-resolution imaging with X-rays is to exploit diffraction. This requires the use of a pencil beam, either by using a pinhole or X-ray focusing optics. An image is then recorded at a relatively long distance downstream of the object, which corresponds to far-field or Fraunhofer diffraction. Images recorded in this way will contain information closely related to the squared modulus of the Fourier transform of the imaged object, convolved with the Fourier transform of the incident beam. It is in certain cases possible to reconstruct the object transmission function by the use of iterative phase retrieval algorithms based on projections onto sets [75–78]. This approach is usually known as coherent diffraction imaging (CDI) [79, 80]. Since the recorded image is in the frequency domain, the attainable resolution is limited by how far from the centre of the detector signal can be measured (and, of course, the wavelength of the probe). In practice, this means that the resolution limit is related to the signal-to-noise ratio in the recorded images. Therefore, very high resolution can be achieved with this technique. CDI is limited to imaging of isolated particles with a support smaller than the used X-ray beam, however, such as isolated nanoparticles [82] or single cells [83].

The small support requirement can be obviated by scanning the probe across an extended sample while letting the probe position overlap at each image position (in practice the sample is scanned through the beam). By using an iterative reconstruction scheme, a complete phase projection can be reconstructed [84–86]. This is known as ptychographic imaging [87].

Since the phase shift introduced by the object in the X-ray beam can be considered as a straight-line projection, if we have access to the phase shift, we can use it to reconstruct the 3D refractive index decrement distribution in the sample, in analogy to the classical attenuation case. What is particularly attractive with this is that for hard X-rays, the refractive index decrement is proportional to the local mass density in the sample [88]. This means that, for example, the use of X-ray phase tomography images to drive mechanical simulations avoids the need to infer the mass density from measurements of the degree of mineralisation of bone (DMB), which has to be done if density is to be related to the attenuation index [9]. In practice, phase tomography is implemented by a two-step process: first, the phase is retrieved at

each projection angle, and then the refractive index decrement is reconstructed by feeding the resulting phase maps into a tomographic reconstruction algorithm such as filtered back projection (FBP) [89–91].

Ptychographic tomography has been used to image bone ultrastructure [81]. A human cortical bone sample cut to an approximately cylindrical shape with a diameter of ~25 μm was imaged using a 2.3 μm pinhole (Fig. 1.2a). The sample was scanned through the resulting pencil beam so that the X-ray spots lie on concentric circles, covering a rectangular area of 40 μm × 32 μm (Fig. 1.2b) for a total of 704 diffraction patterns per projection. Such projections were recorded over a 180° turn of the sample, at increments of 1° for a total of 180 projections.

Figure 1.2c, d shows virtual sections through the reconstructed electron density map. The bright shell on the surface of the sample is due to the sample preparation; the sample was cut using a focused ion beam, which deposits a residue of heavy ions on the surface (in this case gallium ions). We can easily see the lacunae and the canaliculi. Note that the reported electron densities are truly quantitative due to the sample being completely covered by the projections. 3D renderings (Fig. 1.2e, f) show that the imaged volume contains three partial lacunae. The canaliculi are fairly well resolved, but some spurious structures remain.

The major strength of ptychographic tomography is that it is capable of attaining very high resolutions without the use of X-ray optics. Isotropic 3D resolutions up to 16 nm have been reported [92], however, in energy ranges that are probably too low to be practical for bone imaging (~6 keV). A major drawback of ptychographic tomography is its scanning nature. This makes the acquisition time for a single projection relatively long; in practice, it limits the number of projections that can be acquired and the field of view that can be covered. In the work of Dierolf et al. [81], only 180 angular positions were acquired, normally far too few to achieve correct angular resolution, and a relatively small sample was imaged, comprising only parts of three lacunae. The duration of the complete acquisition was reported to be ~40 h. Another disadvantage, shared with the in-line phase imaging (Sect. 5.1.3), is that reconstruction is not always straightforward. Considerable expertise seems to be needed to perform correct reconstructions. These two drawbacks taken together seem to limit the applicability of ptychographic tomography for quantitative studies. Additionally, ptychography can only reconstruct phase shifts in the range 0–2π. This means that if the true phase shift is larger than 2π, the reconstruction has to be unwrapped, which is a problem unto itself [93].

5.1.2 Transmission X-Ray Microscopy (TXM)

Magnification on the X-ray side can be achieved by the implementation of a transmission X-ray microscope, analogously to what can be done with visible light. Due to the weak refraction of X-rays, diffractive optics, so-called Fresnel zone plates, are used for this purpose. A full-field TXM implementation has been reported by Andrews et al. [94], using either a rotating anode X-ray source or a synchrotron source to image bone tissue at the nanoscale. They used a reflective capillary collimator due to its high focusing efficiency. The sample was placed in the focus. A Fresnel zone plate was used as objective lens to image the beam onto the

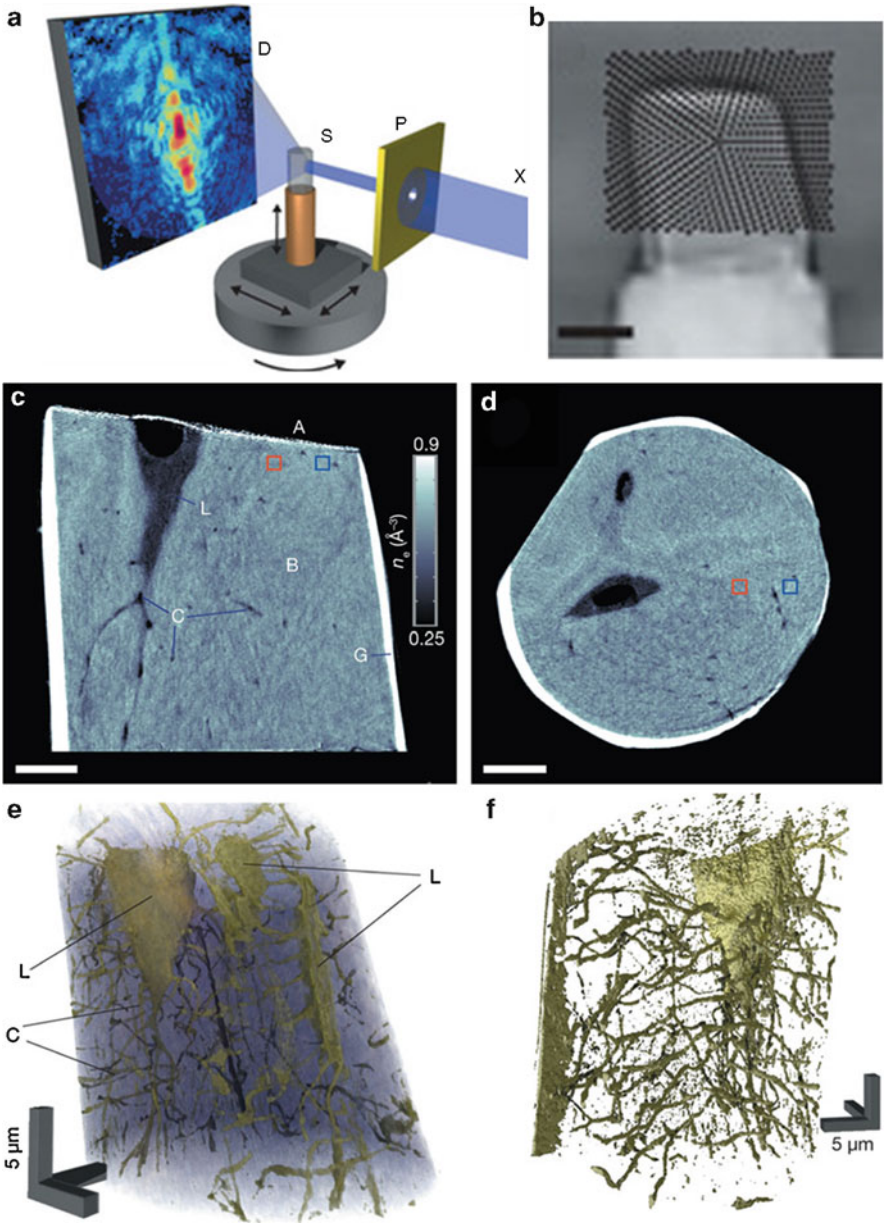

Fig. 1.2 Ptychographic X-ray tomography. (**a**) Schematic of the experimental setup. (**b**) The scanning pattern of the X-ray spot over the sample to form one projection. (**c**, **d**) Virtual cuts through the reconstructed volume showing very good contrast between bone and the LCN. The bright shell consists of gallium ions deposited by the focused ion beam cutting of the sample. (**e**) Volume rendering of the complete imaged volume. Three lacunae can be partially seen, and a fair amount of the canaliculi seem well resolved. (**f**) Zoom on one lacuna and its canaliculi. A fair amount of spurious porosity remains (Images from Dierolf et al. [81])

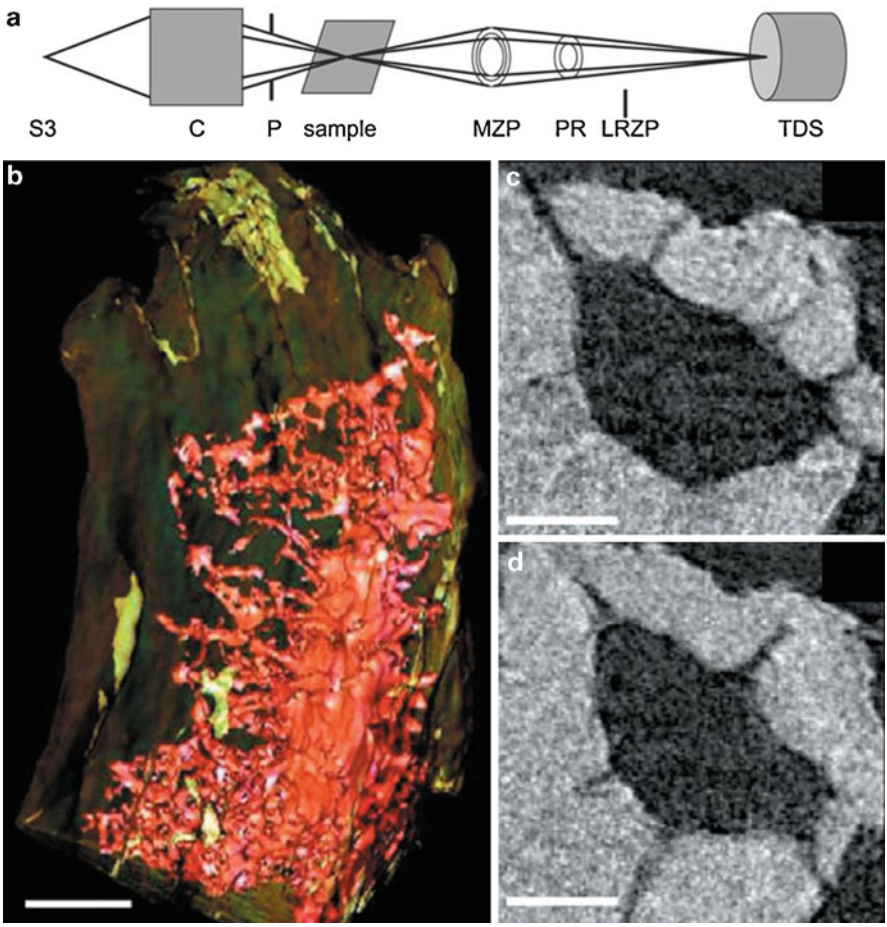

Fig. 1.3 Transmission X-ray microscopy (TXM). (**a**) Schematic of the experimental setup. (**b**) Volume rendering of an osteocyte lacuna in an isolated murine trabecula. (**c**, **d**) Virtual cuts through the reconstructed volume showing the contrast between bone, the lacuna and the canaliculi (Images from Andrews et al. [94])

detector. Detection was done using a scintillator-based high-resolution CCD camera with a physical pixel size of ~2 μm. A schematic of the instrument is shown in Fig. 1.3a. The X-ray energy used was in the range of 4–14 keV. They achieved a spatial resolution of ~50 nm, compared to the theoretical resolution limit of ~35 nm.

The reported TXM setup was used to image the LCN. Part of one lacuna and its environing canaliculi were imaged in trabecular bone. The sample was extracted from the proximal region of a mouse tibia by microtome cutting, followed by washing with a saline jet to remove marrow. It was then dried and attached to a steel cannula tip with epoxy for imaging. The resulting sample consisted of a single trabecula and was less than 50 μm thick, which is approximately the depth of focus

of the TXM. The sample was stained with 1 % uranyl acetate for 12 h to improve contrast. The lacuna and canaliculi are well resolved in the image, but are fairly weakly contrasted (Fig. 1.3c, d). Looking at a volume rendering (Fig. 1.3b), the lacuna and its canaliculi are clearly visible. The canaliculi show a surprising rate of branching, however, compared to the two other techniques reported here.

A TXM images the attenuation of the sample, i.e. the same contrast as in standard X-ray μCT. An advantage of TXM is that it can achieve high spatial resolution without the need for advanced image reconstruction. The disadvantages seem to be the demanding sample preparation and the limited sample size due to the short depth of field, approximately 50 μm. The technique also requires fairly low energies, thereby limiting the thickness of the samples that can be traversed. The lower energy also increases the X-ray dose deposited in the sample, thus increasing the risk of radiation damage.

5.1.3 In-line Phase Tomography

It is possible to implement a transmission projection microscope by the use of X-ray optics to focus the beam and placing the sample after the focus in the resulting divergent beam. This kind of microscope has been implemented using Kirkpatrick-Baez reflective optics [95]. As for the methods discussed above, the sample is placed on a translation/rotation stage to enable tomographic imaging. The camera is mounted on a translation stage to allow for different factors of geometrical magnification. The magnification is a function of the beam divergence after the focus, the focus-to-sample distance and the focus-to-detector distance. The resulting free-space propagation not only creates a magnification effect however, but due to the high degree of coherence of the beam, phase contrast is also induced. This contrast can be used to reconstruct the phase shift in the object. One particularity, however, is that the recorded images will lack information at certain spatial frequencies due to the properties of the transfer function of the Fresnel propagator. In high-resolution imaging, this makes it necessary to acquire several (at least two) images per projection angle, corresponding to different sample-to-detector distances. Another aspect is that bone samples will always introduce a considerable attenuation effect at the energies used in practice. This means that both attenuation and phase contrast will be present in the recorded images, which also imposes a minimum of two images per projection angle. Otherwise, strong assumptions have to be made on the sample composition to make phase retrieval possible.

The phase can be retrieved at each projection angle by a process known as phase retrieval. Several algorithms for phase retrieval from Fresnel diffraction patterns have been developed. Most of them are based on linearisation of the squared modulus of the Fresnel transform to achieve efficient, filtering-based solutions [89, 90, 96–99]. In the high-resolution case, there will be non-negligible non-linear contributions. This makes the use of non-linear reconstruction algorithms necessary to achieve the resolution permitted by the experimental setup (Sect. 4.3) [100–104].

In-line phase tomography has been used to image several ultrastructural features in bone [72]. The LCN can be imaged over a relatively large field of view (Fig. 1.4a–d). The LCN also seems better resolved than then in the previously

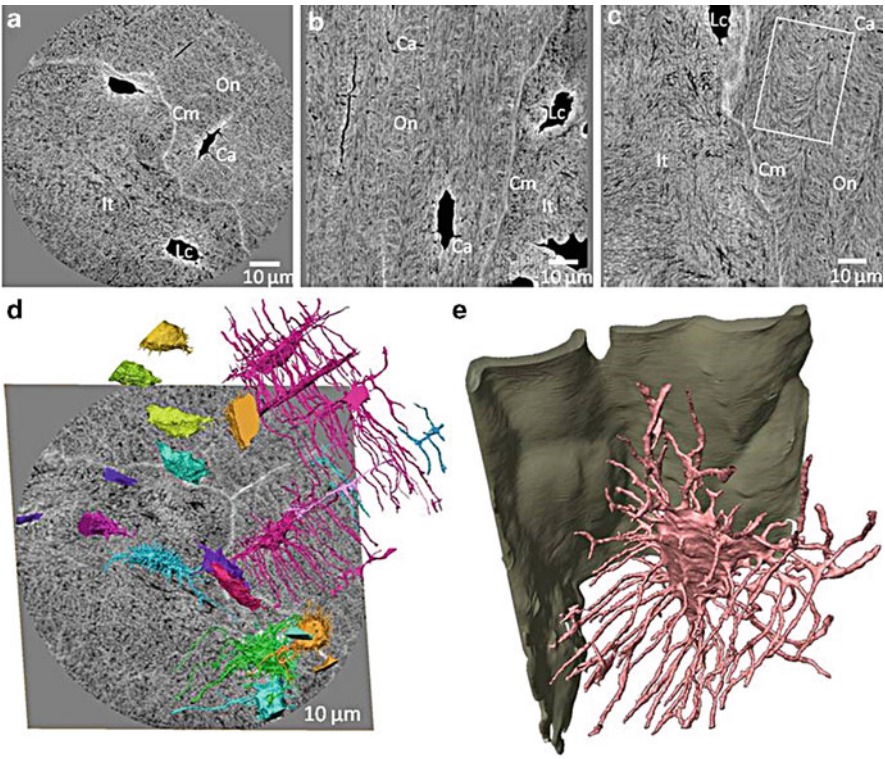

Fig. 1.4 Magnified phase tomography of bone. (**a**–**c**) Virtual cuts through the reconstructed volume. Note the high contrast between the LCN and the bone matrix and also the strong contrast in the matrix presumably due to oblique cutting of the mineralised collagen fibres, as well as the well-resolved cement line. (**d**) Volume rendering of all LCN porosity in the sample showing a relatively large number of lacunae. (**e**) Zoom on one lacuna and its canaliculi (*pink*) and the cement line (*green*). The LCN is rendered in unprecedented detail, and its relationship to the cement line can be studied [72]

reported studies (cf. Figs. 1.2f, 1.3b and 1.4e). The bone matrix appears strongly textured (Fig. 1.4a–c) compared to, e.g. images acquired with X-ray ptychographic tomography (Fig. 1.2c–d). By comparison to qBEI [40] and TEM [44] images, the arching structure can be identified to be due to the oblique cutting of the mineralised collagen fibrils. This means that the collagen fibre orientation can be studied directly in 3D using texture analysis, as we will see below. The cement lines are comparatively very well contrasted. In phase tomography, the reconstructed grey level corresponds to the mass density in non-hydrogen-rich materials. In the images, it can be seen that the cement line has a significantly higher mass density than the surrounding osteonal and interstitial tissue regions.

In-line phase tomography has some aspects that make it attractive for bone imaging. It is a full-field imaging technique, which means that the image acquisition is relatively fast. Acquisition time of ~4 h per sample has been reported [72], using

full sets of projections (i.e. 3000 projections using a 2048-element-wide detector). This means that quantitative studies on large series of samples are potentially within the capabilities of this technique. Further, due to the full-field nature, a relatively large field of view can be imaged compared to the other available techniques.

The in-line technique currently has one disadvantage in common with ptychographic tomography, however. Image reconstruction is not straightforward, since it relies on advanced reconstruction algorithms that presently require considerable expertise to operate. A disadvantage compared to ptychography is currently the achievable spatial resolution. While no measurement has been reported, by inspection of the reconstructed volumes, the spatial resolution so far achieved seems to be ~200 nm (FWHM at interfaces in the reconstructed 3D object). With these advantages and disadvantages taken together, in-line phase tomography seems to be an appropriate method for quantitative studies and study of ultrastructural features in addition to the LCN.

5.2 Collagen Orientation

Three-dimensional images acquired by means of in-line phase tomography allow to explore the details of the submicron-scale architecture of bone. In particular, the structure of bone lamellae can be analysed in unprecedented detail.

Lamellar pattern is the dominating arrangement of bone in the human skeleton and can be found most frequently in the form of osteons. Osteons are approximately 200 μm diameter cylindrical structural units constituted by concentrically arranged lamellae surrounding the central Haversian canal of 50–100 μm diameter hosting blood vessels and nerves. Lamellae are 3–7 μm thick layers that were characterised and defined originally on microscopy images of cut sections. The reason for the appearance of lamellae was already more than hundred years ago proposed to be the ultrastructure, namely, the orientation of the collagen-mineral composite [105].

One interesting question has been – and still is – if the lamellar structure is the result of a collagen self-assembly processes [44, 106] or if it is determined by the activity of the osteoblasts laying down bone tissue, driven through their mechanosensing ability, following a predefined programme or signals sent by osteocytes. However, the major driving force behind studies investigating bone microarchitecture has been the role of these structural details in determining function and vice versa. Ultimately, in-depth knowledge on structure-function relationships may complete our understating of the complex design and remarkable mechanical properties of these highly optimised skeletal elements [107]. The effect of bone diseases on the mechanical competence and the underlying alterations in the composition and architecture are also of great interest. Moreover, the underlying principles may be useful for the design of new materials for mimicking bone tissue [106] or for other bio-inspired engineering purposes.

With respect to the role of ultrastructure in mechanical properties of lamellar bone, besides numerous other studies, the works of Ascenzi and colleagues have to be mentioned. These authors extensively researched and reported the potential

relationships between the osteonal types classified based on appearance under confocal microscopy and mechanical properties of isolated osteons [108–111] and lamellae [111] assessed experimentally. However, understanding the exact architecture of lamellar bone remained a challenging task mainly due to the available tools of investigation. Inference of the three-dimensional arrangement of collagen fibrils and/or mineral particles was attempted from 2D sections acquired mainly by various microscopy techniques [109, 112–119], scattering [120–122] and diffraction based [123], i.e. mainly in reflection or transmission mode. Interpretation of these results therefore required assumptions and theoretical models. Some of these approaches lead to partially or fully misleading conclusions as it was pointed out, e.g. by Giraud-Guille et al. [112]. Using these various methods, several researchers' opinion converged towards the agreement that lamellae have a periodic plywood structure. However, various descriptive models have been proposed including orthogonal [105], twisted [112], rotated [114] and helicoidal [124] plywoods. Furthermore, a remarkably different opinion was formulated by Marotti et al. [125], proposing that the collagen matrix is rather disorganised and the lamellar pattern is the result of neighbouring regions having distinct collagen densities. A potential explanation for these different observations has been provided recently [126]. However, there was a clear need for truly three-dimensional analysis techniques to fully resolve these structural details and explain the partially or fully contradicting findings of previous 2D analyses.

In-line phase tomography provides the density contrast and spatial resolution that are sufficient to investigate and quantitatively describe this complex arrangement in three dimensions.

As pointed out in Sect. 5.1.3, the characteristic arcing pattern apparent in Fig. 1.4a–c is the result of this lamellar structure and was an important basis for previous 2D, e.g. electron microscopy-based analyses attempting to resolve the lamellar structure [112]. Having the 3D data at hand, it is possible to virtually prepare slices in arbitrary directions. Aligning these slices with the lamellar plane allows one to observe the arrangement of collagen fibrils within sub-lamellae. This principle was the basis of the image analysis protocol presented in [127]. In particular, slice-wise autocorrelation analysis was performed to quantify the local orientation of the fibrils. We assumed that the in-plane pattern of the fibrils was quasi-periodic and used the major principal axis of the autocorrelation-based orientation distribution function of periodicity to identify the dominant direction of fibrils within the given plane. Independently assessed results of consecutive parallel slices provided the evolution of the mean orientation of the bone lamellae. Several sub-volumes aligned with the local lamellar coordinate system were investigated.

Using this technique, we confirmed that mineralised collagen fibrils in lamellar bone are organised into a plywood structure that is made of parallel quasi-planes in which the fibrils have unidirectional alignment. Within the largest analysed region, having an in-lamellar-plane dimension of approximately 30×70 µm, the standard deviation of the quantified fibril orientation was as small as five degrees. The evolution of fibril orientation across lamellae was dominated by smooth transitions; discrete changes were rare. We found two major plywood pattern types. The first one

resembled the rotating plywood described earlier [112], with the orientation changing continuously. For the first time, to our knowledge, we quantified the rate of twist and found that it was fairly constant across regions and specimens, being approximately 25°/μm. The range of twist was close to either 180 or 360°. Fibrils completed a 180° twist in approximately 7 μm, which corresponds well with lamellar thickness values reported earlier [128]. In the second lamellar type, the change of fibril orientation followed a closely sinusoidal pattern, with average amplitude of approximately 30° and a relatively small offset, on average seven degrees, around the osteon axis. We called this pattern oscillating plywood and found cases resembling symmetric as well as rather asymmetric sinusoids. The average half period of these sinusoids was close to six microns, which is again close to previously reported lamellar thickness values. This pattern was close to that found earlier [123] in a single sample, however, with a much smaller offset with respect to the osteon axis.

We found twisting and oscillating plywood patterns to coexist within the same osteon in a consecutive manner. Close to the external boundary of the osteon, i.e. at the cement line, we observed in all investigated cases twisting plywood arrangement. The lamellar structure of osteons was hypothesised to have importance mechanically by acting as an efficient crack arresting boundary and thus protect the vessels and nerves within the central canal [107]. Our finding is in line with this hypothesis as twisted plywood contains all fibril orientations and, by means of collagen bridging, may therefore be a general defensive mechanism against cracks in any direction [129] and it is located directly at the external border of the osteon. Furthermore, the outermost lamella, being the firstly deposited one, may be important in the early phase of the construction of the osteon.

As a qualitative validation of our approach, in a selected analysis region, the computed orientation was used to construct a virtual 3D fibril model that compared well with the corresponding sub-volume of the original greyscale image, and, in particular, the arch pattern could be reproduced (Fig. 1.5). The figure illustrates the necessity of 3D analysis as the evaluated complex arrangement displayed in the centre panel of Fig. 1.5 cannot be retrieved from a 2D section, e.g. from the oblique cut shown in the left panel.

Apart from the plywood-type arrangements, we could observe rather disorganised regions [130]; however, these had very rare occurrence. Furthermore, we found that fibrillar orientation was independent of the local mass density values, suggesting that the known fluctuation of mechanical properties across lamellae [117, 131–133] is dominated by the orientation of the fibrils rather than the level of mineralisation.

In summary, our results not only corroborated findings of earlier studies, but provided novel insight into the lamellar microstructure in bone. Further, a unique set of quantitative results could be derived from nanoscale three-dimensional data and allowed reinterpretation of previous observations. Moreover, our findings were in line with the results of the concurrent, but independently performed, studies of Reznikov et al. investigating lamellar arrangement in various species by means of FIB-SEM [42, 60, 134]. This approach is attractive as it provides a resolution of about 10 nm. However, it is limited to a field of view of 10 μm and at the price of full destruction of the sample. Finally, the existence of the two plywood arrangements